Analyst

ROYAL SOCIETY OF CHEMISTRY

PAPER

View Article Online
View Journal | View Issue

Check for updates

Cite this: *Analyst*, 2024, **149**, 2445

Enhanced TNT vapor sensing through a PMMA-mediated AIPE-active monocyclometalated iridium(III) complex: a leap towards real-time monitoring†

Ram Prasad Bhatta, Annu Agarwal, Vishal Kachwal,‡ Pramod C. Raichure § and Inamur Rahaman Laskar *

Based on the explosive nature and harmful effects of nitro-based explosive materials on living beings and the environment, it is extremely important to develop luminescence-based probe molecules for their detection with excellent selectivity and sensitivity. Two AIPE (aggregation-induced phosphorescence emission)-active iridium(III) complexes (**M1** and **M2**) were developed for the sensitive detection of TNT in both contact and non-contact modes. The aggregate solutions of both complexes (**M1** and **M2** in THF/H_2O, 1/9 by volume) detected TNT at the pico-molar (pM) level. These complexes showed greatly enhanced emission intensity while embedded in a PMMA(polymethyl methacrylate) matrix film. The amplified quantum efficiency, improved phosphorescence lifetime, and enhanced porous network of **M2**-PMMA composite helps to improve the sesitivity of TNT vapor detection. Interestingly, the sensitivity of the detection of TNT by the **M2** complex was significantly improved (5-fold) in a PMMA-incorporated complex (CP) with an observed limit of detection (LOD) of 12.8 ppb. From the BET analysis of CP, it was observed that the mesoporous network of CP has an average pore diameter of 8.52 nm and a surface area of 2.03 m^2 g^{-1}. The porous network of CP assists in trapping TNT vapor in a polymeric network containing an electron-rich probe (iridium(III) complex, **M2**), which helps to effectively trap TNT, thus enhancing electronic communication. As a result, significant emission quenching was observed.

Received 19th December 2023,
Accepted 26th February 2024

DOI: 10.1039/d3an02184j

rsc.li/analyst

1. Introduction

In recent years, convenient methods for detecting nitro-based explosive compounds with high selectivity and sensitivity have become an area of significant interest since these compounds pose a potential threat to humanity and the environment. Among these compounds, 2,4,6-trinitrotoluene (TNT) is one of the most extensively utilized in military operations and terrorist attacks owing to its stability under ambient conditions.[1,2] The widespread use of TNT leads to significant environmental implications and, therefore, TNT has been recognized as a major water pollutant. These attributes of TNT lead to its easy handling. Thus, it is increasingly used by terrorists in making life-threatening weapons, triggering a serious concerns for homeland security. Moreover, it is a contaminant of water bodies, with permissible concentrations in drinking water limited to 2 ppb because of its risk to the liver, eyes, and nervous system.[3] Therefore, it is kept under the category of priority pollutants by the United States Environmental Protection Agency (USEPA),[3–6] and the sensitive detection of TNT in water bodies and in the vapor phase is highly desirable.

In general, nitro-based explosives have a low vapor pressure (10^{-5}–10^{-15} torr). In the case of TNT, the vapor pressure is 5.8 × 10^{-6} Torr (~10 ppb) at 25 °C, which makes it challenging to identify it in the vapor phase.[7] Many approaches have been used to detect TNT, such as chromatography, mass spectrometry, Raman spectroscopy, X-ray imaging, thermal neutron analysis, electrochemical assays, and ion mobility spectroscopy.[8] The equipment required for these procedures is expensive, heavy, and difficult to monitor in real-time applications.[9,10] Fluorescence-based techniques have a distinct set of advantages, such as greater sensitivity, low cost, and convenience in fabricating portable devices for onsite and real-time detection. Many fluorescence-based probe molecules have been developed for the detection of TNT in the solution phase with high sensitivity, even at the parts per quadrillion (ppq) level.[11–19] However, vapor phase sensing presents many

---

Department of Chemistry, Birla Institute of Technology and Science, Pilani Campus, Pilani, Rajasthan 333031, India. E-mail: ir_laskar@pilani.bits-pilani.ac.in

† Electronic supplementary information (ESI) available. See DOI: **https://doi.org/10.1039/d3an02184j**

‡ Present address: Department of Engineering Science, University of Oxford, Oxford OX1 3PJ, UK.

§ Present address: Department of Chemistry, Indian Institute of Technology (IIT), Bombay, Mumbai, India 400076.

challenges, such as exceptionally low vapor pressure (10^{-5}–10^{-15} torr), and the demands for detecting hidden explosives in transportation hubs and war zones create a complex landscape that is difficult to navigate.[20–24] The scientific community thus finds itself in urgent need of a fluorescence-based probe that is highly sensitive and selective for the detection of TNT in the vapor phase. The key attributes of a robust probe include the appropriately aligned LUMO levels of the probe molecule and analyte for effective electron transfer, significant overlap of the absorption spectrum of the analyte and the emission spectrum of the probe molecule for efficient energy transfer, an extended excited state lifetime of the probe to maximize the interaction time with the analyte, a high quantum yield, and the integration of a porous medium to trap the elusive vapors of the explosives.[24] In the quest to detect nitro-based explosive compounds, various luminescent explosive sensors have been developed, leveraging small molecules, conjugated polymers, self-assembled organic nanomaterials, and metal–organic frameworks.[13,14,25–34] These have been evaluated for their utility in both solution and vapor-phase sensing, but very few reports for fluorescence-based molecules have been employed to detect TNT vapor.[14,19,25,34–36] Mothika and co-workers reported films of tetraphenylene ethylene-based conjugated microporous polymers (PTPETCz) through an electro-polymerization method using tetra(carbazolylphenyl)ethylene monomer, which can detect TNT vapor even at a very low concentration of 33 ppb. In that report, the authors used a custom-made set-up with attached heating coils for the probe as well as the analyte and maintained a temperature of 35 °C for generating TNT vapors. Despite these advancements, the selective vapor sensing of TNT under atmospheric conditions, particularly at a detection limit that would be considered satisfactory (lower ppb to ppt), remains an elusive goal.

Phosphorescent transition-metal complexes have been considered potential candidates in various fields such as chemosensors,[37–41] optoelectronic materials,[42–44] biological probes,[45,46] *etc*. The role of heavy metals like osmium(II) (Os), platinum(II) (Pt), and iridium(III) (Ir) as triplet emitters in these probes is highly desirable. Among these metals, iridium(III) complexes are highly impactful, primarily due to their superior emission properties because of strong spin–orbit coupling (3909 cm^{-1}).[47,48] Moreover, the superior photothermal stabilities and colour tuneability as compared to ruthenium(II) and osmium(II) complexes, and their high coordination number relative to platinum(II) complexes, provide the iridium(III) complexes with a better platform for the structural modifications. 'Aggregation-induced Phosphorescence Emission' (AIPE)-active iridium(III) complexes have emerged as a promising avenue in this quest; their desirable photophysical properties include a significant Stokes shift, high emission efficiency, and relatively extended excited state lifetime.[49–51] Their versatility has found applications in diverse fields such as light-emitting diodes, therapy, and sensing.[50–55]

In 2015, our group (Alam *et al.*) developed mono-cyclometalated AIPE-active iridium(III) complexes and studied their potential for picric acid detection.[51] Recently, our group (Agarwal *et al.*) synthesized a series of AIPE-active Ir(III) complexes and used them to successfully sense different nitro-based explosives.[41] It was observed that tuning the electronic substituents on phenyl pyridine ligands modulates their sensitivity and selectivity towards different nitro-based explosives. One of the complexes having moderately electron-withdrawing substituents (COOH) was found to be sensitive towards TNT in contact mode (LOD −3.6 ppb) based on the PET mechanism. In our study, we have ventured into this exciting terrain to design and synthesize the two new mono-cyclometalated AIPE-active iridium(III) complexes (**M1** and **M2**) by using electron-donating (OMe) and highly electron-withdrawing (CN) substituents on the phenyl ring of the phenyl pyridine ligand, to explore their potential in the sensing of TNT. Initially, we investigated the sensing of TNT in contact mode and found the limit of detection to be in the pM (ppt) range. This impressive sensitivity emboldened us to test our probes for TNT vapor phase sensing. To further improve the sensitivity and stability of the probe, we made the strategic decision to impregnate the probes in a porous PMMA polymer. This decision yielded impressive results, *i.e.*, the post-impregnated probes exhibited quantum yields and lifetimes that were enhanced as compared to the original probe. Then, the preparation of various films from the polymer-impregnated complex (CP) and exposure to nitro-based explosive vapors were carried out. The results were resoundingly positive: the probes demonstrated an uncanny ability to selectively sense TNT vapors with a high level of sensitivity, achieving a detection limit of 12.8 ppb. These findings affirm the potential of our approach and lay the foundation for further advancements in the field.

2. Experimental section

Materials and methods

All materials used were commercially available and were used without further purification. Iridium(III) salt was purchased from TCI, India. 2-Ethoxyethanol was purchased from Sigma Aldrich. The common salts (*e.g.*, sodium carbonate, potassium carbonate, sodium chloride) were purchased from Merck. Boronic acids were purchased from Sigma Aldrich and TCI, and 2-bromo pyridine was purchased from Alfa Aesar. 4-(2-Pyridyl)benzaldehyde was purchased from TCI India. Triply deionized water was used throughout this research work. UV-grade organic solvents were purchased from Spectrochem and used without further purification. ^{1}H NMR, ^{13}C NMR, and ^{31}P NMR spectra were recorded using a 400 MHz Brucker NMR spectroscope. Infrared spectra were recorded on a Shimadzu IR Prestige 21. UV-VIS absorption spectra were recorded using a Shimadzu Spectrophotometer (model UV-1800 and 2550). Steady-state photoluminescence (PL) spectra were recorded on a Horiba Jobin Yvon Spectrofluorometer (FluoroMax-4). Cyclic voltammetry (CV) measurements were carried out on a CH instrument (CHI601E) by using tetrabutylammonium hexafluorophosphate (NBu_4PF_6) as a supporting electrolyte in THF

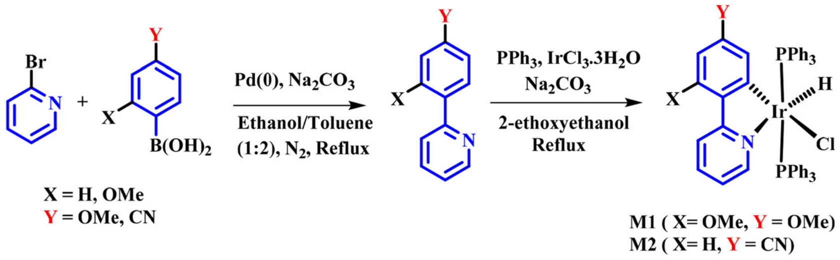

Scheme 1 The general synthesis route for ligands and their corresponding complexes **M1** and **M2**.

solvent at a scan rate of 100 mV s^{-1}. The glassy carbon electrode was used as a working electrode, Ag/AgCl as a pseudo reference electrode, and Pt as a counter electrode were used for the experiment. The particle sizes of the 0% and 90% solutions of **M1** and **M2** were determined on a Malvern Zetasizer (MAL1040152). The quantum yields of the complexes were obtained on a Quanta-Phi (F-3029) instrument. The lifetimes of the complexes were recorded on Horiba Delta Flex 01. An "Apreo LoVac, FEI" FESEM (field emission scanning electron microscopy) instrument was used to record the morphology of the samples. A Quantachrome® ASiQwin™- Automated Gas Sorption Data Acquisition and Reduction © 1994-202 instrument was used for BET analysis. Thermogravimetric analysis (TGA) was performed using TGA-50, SHIMADZU equipment at 10 °C min^{-1}, under a nitrogen atmosphere.

Synthesis and characterisation

Synthesis of ligands. L1: (2,4-dimethoxyphenyl) boronic acid (1.1 mmol) and 2-bromopyridine (1 mmol) were taken in a clean and dry two-necked round bottom flask. A solvent mixture of toluene : ethanol (2 : 1) was added to the round bottom flask and the mixture was purged with nitrogen for 5–10 minutes. Palladium(0) tetrakis(triphenylphosphine) (0.0015 mmol) was added in an inert atmosphere under stirring. Sodium bicarbonate (2.1 mmol) in water was added after 10 minutes of catalyst addition. The reaction mixture was refluxed for 15 hours with intermittent TLC observation. After completion of the reaction, the reaction mixture was cooled to room temperature, water was added, and the compound was extracted in ethyl acetate twice. The organic layer was collected and purified by column chromatography using silica (mesh 60–120) and hexane and ethyl acetate (9 : 1) as a solvent system. A brownish solid product was obtained with an 80% yield (Scheme 2). The ligand was characterized by NMR and HRMS (the spectra are shown in Fig. S1, S2, and S11, ESI†).

^{1}H NMR (400 MHz, chloroform-*d*) δ 8.68 (dd, J = 4.9, 1.9, 1.0 Hz, 1H), 7.86–7.75 (m, 2H), 7.69 (dd, J = 8.1, 7.4, 1.9 Hz, 1H), 7.17 (m, J = 7.4, 4.9, 1.2 Hz, 1H), 6.64 (dd, J = 8.5, 2.4 Hz, 1H), 6.58 (d, J = 2.4 Hz, 1H), 3.88 (s, 3H), 3.87 (s, 3H).

^{13}C NMR (101 MHz, chloroform-*d*) δ 161.33, 158.11, 155.90, 149.30, 135.61, 131.98, 124.74, 122.11, 121.14, 105.06, 98.89, 55.59, 55.46.

HRMS calculated: $[M + H]^{+}$: m/z = 215.0946; found: $[M + H]^{+}$: m/z = 216.1051.

L2: (4-cyanophenyl) boronic acid (1.1 mmol) and 2-bromopyridine (1 mmol) were taken in a clean and dry two-necked round bottom flask. A solvent mixture of toluene and ethanol (2 : 1) was added to the round bottom flask and the mixture was purged with nitrogen gas for 5–10 minutes. Palladium(0) tetrakis(triphenylphosphine) (0.0015 mmol) was added in an inert atmosphere under stirring. Sodium bicarbonate (2.1 mmol) in water was added after 10 minutes of catalyst addition. The reaction mixture was refluxed for 15 hours with intermittent TLC observation. After the completion of the reaction, we isolated the product by following the same process as for **L1**, and the solid product was obtained with an 85% yield (Scheme 3). The ligand was characterized by NMR and HRMS (the spectra are shown in Fig. S3, S4, and S12, ESI†).

^{1}H NMR (400 MHz, chloroform-*d*) δ 8.83–8.73 (m, 1H), 8.13 (d, J = 8.3 Hz, 2H), 7.83 (dd, J = 7.4, 1.8 Hz, 1H), 7.83–7.72 (m, 3H), 7.39–7.31 (m, 1H).

^{13}C NMR (101 MHz, chloroform-*d*) δ 155.22, 150.06, 143.47, 137.16, 132.59, 127.48, 123.39, 121.04, 118.84, 112.45.

HRMS calculated: $[M + H]^{+}$: m/z = 180.0687; found: $[M + H]^{+}$: m/z = 181.0785.

Synthesis of the complexes. M1: iridium(III) salt ($IrCl_3{\cdot}6H_2O$) (1 mmol) and triphenylphosphine (3 mmol) were taken in a 10 ml round bottom flask and refluxed in 2-ethoxyethanol for 4–5 hours. A pale-yellow salt was formed. **L1** (1 mmol) was

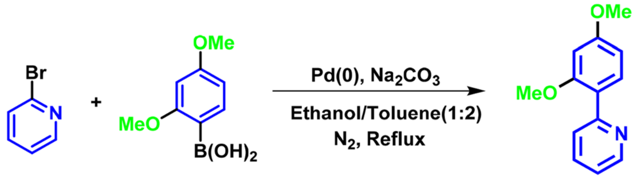

Scheme 2 The synthesis of ligand **L1**.

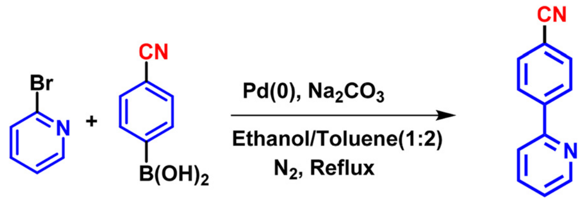

Scheme 3 The synthesis of ligand **L2**.

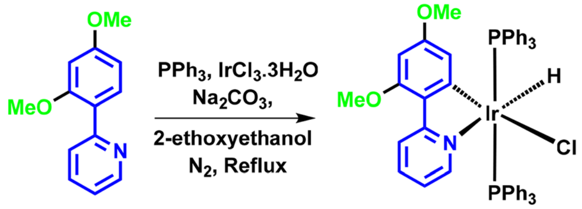

Scheme 4 The synthesis of metal complex **M1**.

added, followed by sodium bicarbonate (1.1 mmol) as a base, and the mixture was further refluxed for 1 hour; the progress of the reaction was monitored by TLC. The reaction mixture was cooled to room temperature (RT) followed by the addition of hexane, and then the solvent was decanted. The crude complex was washed with hexane and diethyl ether 2–3 times and then dissolved in DCM. The dissolved complex was filtered and then recrystallized in a DCM and hexane solvent system. A blue emissive product was obtained with a 76% yield (Scheme 4). The complex was characterized by NMR, HRMS, and IR (spectra shown in Fig. S5–S7, S13 and S15, ESI†).

^{1}H NMR (400 MHz, chloroform-*d*) δ 8.15 (dd, J = 8.3, 1.2 Hz, 1H), 7.70 (dd, J = 12.0, 8.2, 1.4 Hz, 1H), 7.61–7.53 (m, 1H), 7.49 (dd, J = 8.4, 6.8, 3.1 Hz, 1H), 7.39 (dd, J = 7.2, 6.0, 4.3 Hz, 11H), 7.26 (d, J = 7.2 Hz, 1H), 7.21 (t, J = 7.3 Hz, 6H), 7.16–7.08 (m, 11H), 6.58 (dd, J = 7.1, 5.6, 1.4 Hz, 1H), 5.76 (d, J = 2.3 Hz, 1H), 5.32 (d, J = 2.3 Hz, 1H), 3.83 (s, 3H), 2.92 (s, 3H), −16.45 (t, J = 17.1 Hz, 1H).

^{13}C NMR (101 MHz, chloroform-*d*) δ 164.56, 161.16, 158.52, 154.62, 149.49, 135.20, 134.21 (t, J = 5.4 Hz), 132.17, 132.08, 131.98, 131.96, 131.69, 131.43, 128.95, 128.59, 128.47, 127.16 (t, J = 4.8 Hz), 124.42, 121.46, 118.66, 92.05, 54.86, 54.20, 79.16.

^{31}P NMR (162 MHz, chloroform-*d*) δ 10.397, stretching frequency of the Ir–H bond = 2127 cm^{-1}.

HRMS calculated: [M + H]$^+$: *m*/*z* = 967.2087; found: [M + H]$^+$: *m*/*z* = 969.2034.

M2: iridium(III) salt ($IrCl_3{\cdot}6H_2O$) (1 mmol) and triphenylphosphine (3 mmol) were taken in a 10 ml round bottom flask and refluxed in 2-ethoxyethanol for 4–5 hours. A pale-yellow salt was formed. **L2** (1 mmol) was added, followed by sodium bicarbonate (1.1 mmol) as a base, and refluxed for 1 hour. The product was isolated using a similar procedure to that for **M1**. A greenish-yellow emissive product was obtained with a 78% yield (Scheme 5). The structure of the compound was characterized by NMR, HRMS, and IR (spectra shown in Fig. S8 to S10, S14 and 15, ESI†).

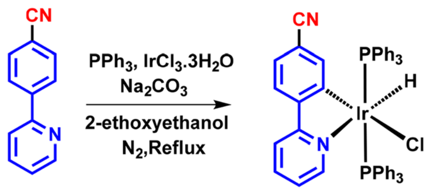

Scheme 5 The synthesis of metal complex **M2**.

^{1}H NMR (400 MHz, chloroform-*d*) δ 9.08 (d, J = 5.6 Hz, 1H), 7.54 (d, J = 8.1 Hz, 1H), 7.48 (td, J = 7.7, 1.6 Hz, 1H), 7.43–7.34 (m, 12H), 7.28–7.19 (m, 7H), 7.15 (tt, J = 6.9, 1.4 Hz, 12H), 6.86–6.76 (m, 2H), 6.40 (d, J = 1.6 Hz, 1H), −16.87 (t, J = 16.7 Hz, 1H).

^{13}C NMR (101 MHz, chloroform-*d*) δ 163.70, 150.78, 150.38, 146.66, 146.17, 135.99, 133.88 (t, J = 5.5 Hz), 131.67, 131.41, 131.14, 129.39, 127.45 (t, J = 4.9 Hz), 122.13, 121.68, 119.23, 118.37, 112.37.

^{31}P NMR (162 MHz, chloroform-*d*) δ 7.118, stretching frequency of Ir–H bond = 2137 cm^{-1}.

HRMS calculated: [M + H]$^+$: *m*/*z* = 932.1828; found: [M + H]$^+$: *m*/*z* = 931.1869.

Sample preparation for sensing

Solution phase detection. The "Aggregation-induced Phosphorescence Emission" (AIPE)-active solutions of both complexes were prepared. Stock solutions of **M1** and **M2** (10^{-3} M in THF) were prepared first, and then 0.5 ml of each complex solution was taken in a glass vial of 5 ml volume. For preparing the 0% water fraction, 4.5 ml of THF was added, and for making the 90% water fraction, 4.5 ml of water was added. The total volume was made up to 5 ml. The 90% water (f_w) in the mixed solvent (THF/water) was directly used for the contact mode detection of TNT.

Vapor phase detection. Both complexes were dissolved in chloroform (10^{-3} M solution), and directly applied to the Whatman filter paper with dimensions 1 cm × 2 cm by dipping paper strips into the complex solution, then the soaked paper was air dried for 12 h and used to record the PL spectra. Similarly, to prepare the PMMA-embedded iridium(III) complex, a mixture containing 5 mg iridium(III) complex and 95 mg PMMA in 10 ml chloroform was sonicated for 15–20 min, then the filter paper strip was dipped into the iridium complex–PMMA mixture solution. The paper strips were dried for 12 hours and then used for sensing applications.

For TNT vapor saturation, 200 mg of TNT crystals were placed in an airtight glass vial of 5 ml capacity overnight at 25 °C to obtain saturated vapors of TNT. Filter paper (FP) is a cheap substrate that is easy to handle for use as the coated probe material. Initially, FP was cut into 1.0 cm × 2.0 cm pieces and coated with the probe material (**M1** and **M2**) by simply dipping the filter paper in a solution of the complexes (10^{-3} M solution in chloroform), air dried, and used to record the PL spectra. The probe (**M1** and **M2**)-coated filter paper was held on the top of a glass vial with saturated TNT vapors (Fig. S29c, ESI†).

A study of the restricted intramolecular rotation (RIR) mechanism

We prepared 10^{-4} M solutions of complexes **M1** and **M2** in THF, and 0.5 ml of stock complex solution was taken in a glass vial of 5 ml capacity. For making 0% polyethylene glycol (PEG), 4.5 ml of THF was added to make the total volume 5.0 ml. Similarly, to prepare 60% PEG, to a 0.5 ml stock solution of complex, 3.0 ml of PEG and 1.5 ml of THF were added, and for

90% PEG, 4.5 ml PEG in 0.5 ml stock solution of THF was added. The recorded photoluminescence spectra and the corresponding photoluminescence image of the prepared solution under UV excitation (365 nm) are shown in Fig. S18, ESI†.

Limit of detection (LOD) calculation

A series of fluorometric quenching titrations were carried out for the detection of TNT by using synthesized complexes (**M1** and **M2**) in the solution phase as well as the vapor phase. The limit of detection (LOD) was determined in both complexes by using the standard method ($3\sigma/M$).[34] Here, σ is the standard deviation of 10 blank measurements and M is the slope from the Stern–Volmer (S–V) plot. We repeated all the titrations three times. Each S–V plot was plotted for I_0/I *versus* the concentration of analyte, where I_0 is the intensity of the initial fluorophore in the absence of a quencher, and I is the intensity change with the subsequent addition of a quencher. The standard deviation of three measurements was calculated as an error and shown as an error bar for all the S–V plots.

Computational studies

To gain insight into the distribution of electrons in the complexes, Density Functional Theory (DFT) calculations were performed using the Gaussian 16 package.[56,57] As both the complexes have iridium(III) as a heavy metal, PBEPBE was used as a functional and LANL2DZ as a basis set.[58] All the computational studies were done in the gaseous state. The optimized structure with HOMO–LUMO distribution is shown in Fig. S39, ESI†.

Electrochemical properties

Cyclic voltammetry (CV) measurements were performed on an electrochemical analyser from CH instruments in a 10^{-4} M THF solution of the complexes using tetrabutylammonium hexafluorophosphate as a supporting analyte under an inert atmosphere. An Ag/AgCl electrode was used as a reference electrode, a platinum wire as a counter electrode, and a platinum electrode as the working electrode. All measurements were performed with a scan rate of 0.1 V s^{-1} and a 0.1 M concentration of the supporting electrolyte was used throughout the experiment. Every solution was degassed with nitrogen bubbling before performing the experiment.

The HOMO and LUMO energy levels for **M1** and **M2** were determined from the equation $E_{\text{(LUMO)}} = E_{\text{(HOMO)}} + E_{\text{(gap, electronic)}}$. The energy gap between the HOMO and LUMO levels was determined from the band-edge absorption of the UV-VIS spectrum. The HOMO energy $E_{\text{(HOMO)}}$ was calculated from cyclic voltammetry (CV) for both complexes.

Thin film formation for lifetime, quantum efficiency, and BET analysis

Solid samples of both complexes (**M1** and **M2**) were dissolved in chloroform (10^{-3} M) and deposited on a glass coverslip through drop-casting and dried in a vacuum oven at 60 °C for 24 h. The dried film was used for measuring the excited state lifetimes and quantum yields (with the help of an integrating sphere) of complexes. Similarly, to prepare the PMMA-embedded iridium(III) complex, the mixture of 5 mg iridium(III) complex and 95 mg PMMA in 10 ml chloroform was sonicated for 15–20 min. The PMMA-complex solution was spread on a glass coverslip through drop-casting and dried in a vacuum oven at 60 °C for 24 h. The dried film was used for recording excited state lifetime and quantum yield measurement. The PMMA-embedded complex films were prepared in large quantities and were cut into small pieces and used for BET analysis.

X-ray single-crystal diffraction study

Single-crystal data for **M2** were collected using a Rigaku Oxford XtaLAB diffractometer using Mo-Kα (λ = 0.709 Å) radiation, and the collected data were processed with the CrysAlisPRO 2021 software.[59] The structure determination was carried out with the SHELXT program, and data refinement was done using SHELXL programs embedded in OLEX^2-1.51.[60,61] All non-hydrogen atoms were refined anisotropically by the full-least-squares method, whereas all the hydrogen atoms were refined isotopically.

3. Results and discussion

The synthesis of ligands was conducted *via* the Suzuki coupling of 2-bromopyridine with boronic acid-substituted phenyl analogues. These ligands were then used to synthesize mono-cyclometalated (C^N) complexes of iridium(III)[52] (Scheme 1). The detailed synthetic procedures for ligands and complexes are described in the Experimental section. The complexes were obtained with good yields (>70%) and were characterized by ^{1}H, ^{13}C, ^{31}P-NMR, HRMS, and IR spectroscopy (see data in the Experimental section and ESI, Fig. S1–S15†).

Photophysical properties

The absorption spectra of the complexes were recorded in THF solvent at room temperature (Fig. 1a). Here, three absorption bands were observed for the cyclometalated complexes of iridium(III) (**M1** and **M2**), which is in line with the previous reports (the absorption spectrum of the unsubstituted complex is shown in Fig. S17, ESI†).[24,51] The intense lowest wavelength transition for both complexes was at 290 nm, which is primarily due to $^1\pi$–π^* transitions centred in the cyclometalated ligand as observed in the unsubstituted complex (Fig. S17 ESI†). The middle-range transitions (320–400 nm) are attributed to the mixed $^3\pi$–π^* transitions and spin-allowed ^{1}MLCT (metal-to-ligand charge transfer) transitions, which were centred at ∼330 and ∼380 nm for **M1** and **M2**, respectively. For **M1**, these transitions started at 374 nm and extended to 404 nm, which might be due to the mixing of the ^{1}MLCT and ^{3}MLCT.[62,63] Similarly, for **M2**, the combined ^{1}MLCT and ^{3}MLCT peak was observed at 413 nm, which extended to 490 nm. A bathochromic shift was observed because of the electron-withdrawing substituent on the phenyl pyridine ligand of **M2**. It stabilized the LUMO of **M2**, which in

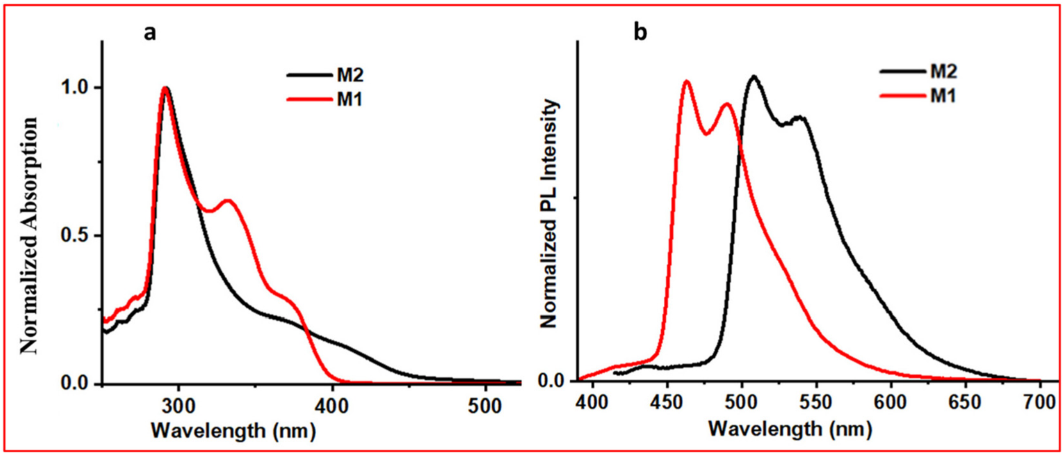

Fig. 1 (a) UV-visible spectra (10^{-6} M solution in THF) and (b) PL spectra (10^{-3} M solution in THF) of both the complexes.

turn shifted the absorption to a longer wavelength as compared to the **M1** complex.

Here, 10^{-3} M solutions of iridium(III) complexes were prepared in THF solvent to record the emission spectra (Fig. 1b). The observed structured emission suggests that the lowest excited state will have a predominantly ligand-centered transition.[63,64] On exciting at 370 nm, Ir 2OMe (**M1**) produced an emission with λ_{max} of 492 nm, which is in accordance with its bluish emission colour under a UV lamp. On substitution of the phenyl pyridine with an electron-withdrawing group (–CN), the value of λ_{max} in the emission spectrum was shifted bathochromically by 47 nm with respect to **M1**, which showed a greenish emission (λ_{max} ~539 nm). On recording the excited state lifetime of both complexes, these were observed in the μs range (**M1**–7.5 μs and **M2**–8.8 μs, ESI, Table S1†), suggesting that they are phosphorescence-emitting molecules.

We were able to grow single crystals of one of the complexes (**M2**) in a DCM/hexane (1 : 1) mixture through the diffusion technique (**M2**, CCDC 2314849). The ORTEP diagram for **M2** showed a distorted octahedral geometry at the Ir(III) site. Asymmetric units contain two molecules. The crystal packing with crystal voids present in the crystal lattice is shown in Fig. 2. The presence of propeller-shaped triphenylphosphine molecules in a crystal packing led to the void space in the crystal packing. The crystallographic data is presented in Table S3, ESI†.

We investigated the 'Aggregation-induced Phosphorescence Emission' (AIPE) properties of both complexes in the mixed tetrahydrofuran and water solution. In a solution of THF, the complexes showed very weak emission. An increase in photoluminescence intensity was observed when the water concentration was gradually increased (Fig. 3). Photographs of the AIPE study under a 365 nm UV excitation and a plot of PL intensity at 0% water to 90% water are shown in Fig. 3, inset. Additionally, a PEG and THF experiment was conducted to verify the restricted intramolecular rotations (RIR) of PPh_3 units in the complexes (Fig. S18, ESI†). The gradual enhancement of emission with increasing PEG concentration supports that the RIR effect might be responsible for AIPE. The AIPE occurs because of the limited rotation of phenyls in triphenylphosphines, known as restricted intramolecular rotation (RIR). This phenomenon is evidenced by the crystal packing diagram of **M2**, which displays C–H⋯π interactions and several short contacts with distances ranging from 2.35–2.85 Å (Fig. S19, ESI†). The phenyls in triphenylphosphines participate in these short contacts, which restrict the rotation of propeller-shaped triphenylphosphines in the solid state. As a result, non-radiative pathways are blocked, leading to AIPE activity in the solid state. A DLS study for particle size analysis was performed for 0% and 90% water for both complexes (Fig. S20, ESI†). For **M1**, the observed particle size for 0% was 22.3 nm, and that for 90% was 231.9 nm. For **M2**, the observed particle size was 38.9 nm for 0% and 165.8 nm for 90% solution.

The reported iridium(III)-based monocyclometalated complexes showed AIPE active properties with high quantum yields and phosphorescence lifetimes.[65] Thus, we have analysed the excited state lifetimes and quantum yields (QY) of both complexes in the solid state (Table S1, ESI†). **M1** had an absolute QY of 23.8% and a lifetime of 7.5 μs, while **M2** had a QY of 33.6% and a lifetime of 8.8 μs. The observed high QY and lifetime data also indicate the potential of these complexes towards the sensing of analytes. The synthesized complexes **M1** and **M2** were tested in their ability to sense different nitro-based explosives by using probe-coated filter paper strips (Fig. S21(a) and (b), ESI†). The results showed that **M1** is selective towards both TNP and TNT, while **M2** is selective towards TNT. The selectivity of **M2** in the AIPE-active solution was also tested (Fig. S21(c), ESI†), and it showed selectivity towards the TNT analyte. We also performed the anti-interference study of **M2** in the presence of different nitro-based analytes for TNT sensing experiments as shown in a bar graph (Fig. S21(d), ESI†). It was found that the quenching performance of **M2** was not affected by the presence of various analytes. Thus, the synthesized complexes were used for sensing TNT in an aqueous medium. An aqueous solution of TNT (10^{-4} M) was added to the aggregate solution (90% water) of **M1** (addition: 1.0 nM

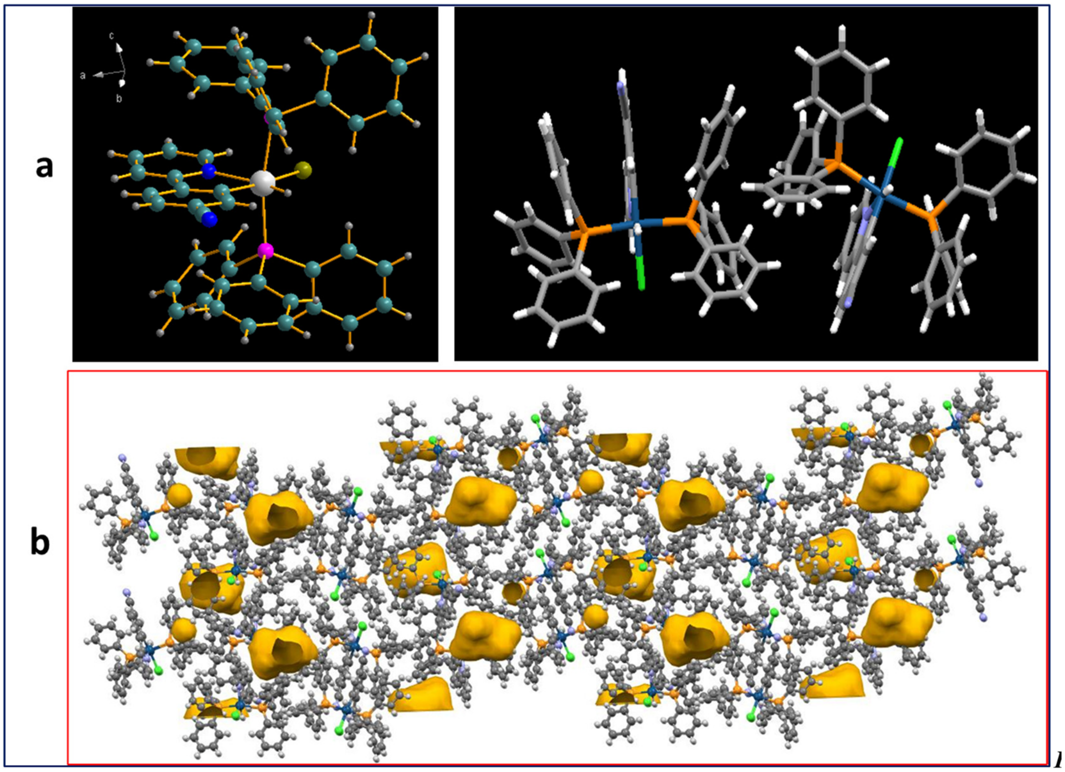

Fig. 2 (a) The ORTEP diagram for **M2** (left) and the asymmetric unit of the complex having two molecules of **M2** (right). (b) The crystal packing diagram showing crystal voids (filled with yellow colour).

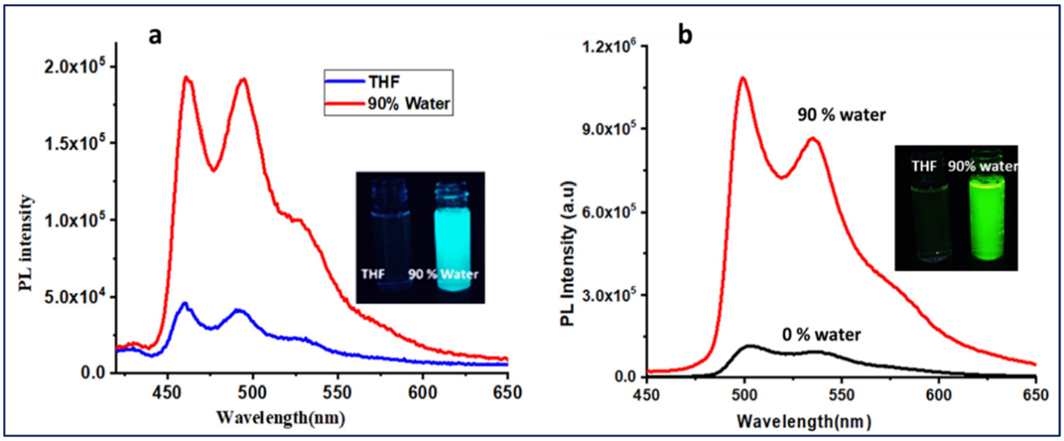

Fig. 3 The probe in THF (10^{-4} M) and its aggregate solution (90% water): (a) PL spectra of the probe in THF (0% water, blue line) and its aggregate solution (90% water, red line) in the case of the **M1** complex. (b) PL spectra of the probe in THF (0% water, black line) and its aggregate solution (90% water, red line) in the case of the **M2** complex. The inset images represent the emissions of the respective probe solutions under UV irradiation (λ_{ex} = 365 nm).

each time up to 14 nM). The emission spectrum of each solution was recorded (Fig. 4 for **M1**). Similarly, the initial emission spectrum of the aggregate solution of **M2** was recorded, then titrated with aqueous TNT (10^{-5} M) by gradually adding 0.5 nM each time and recording the change in the emission intensity (Fig. 5 for **M2**). It was observed that in the case of **M1**, the limit of detection (LOD) was 1091 pM (1.091 ppb) and in the case of **M2**, the LOD was 450 pM (450 ppt). The Stern–Volmer (SV) plot (Fig. S22, ESI†) showed a linear relationship at a lower concentration; moreover, it bent upward as the concentration of TNT increased. Considering the lower concentration plot, the quenching constant (K_{SV} in M^{-1}) was calculated for both complexes (1.49×10^8 M^{-1} for **M1** and 2.5×10^8 M^{-1} for **M2**). This non-linear S–V plot indicated that PL

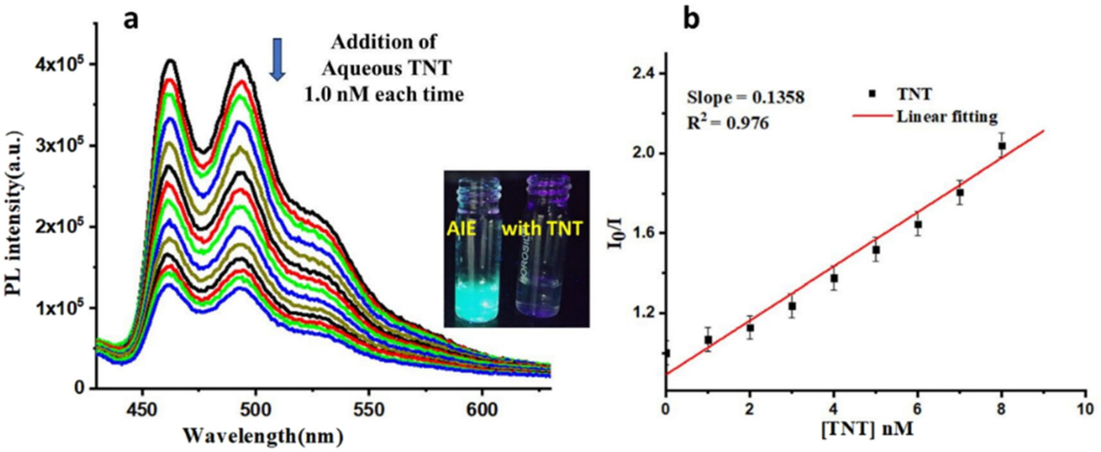

Fig. 4 (a) PL spectra showing a decrease in the photoluminescence (PL) intensity of the AIE solution of **M1** (10^{-3} M THF (10%) and water (90%)) with the continuous addition of aq. TNT (1.0 nM) each time. Inset: the 1st vial contains the aggregate (90% water) solution of the probe, and the 2nd vial contains the aggregate solution of the probe with TNT. (b) Stern–Volmer plot of emission quenching for **M1**; the error bars represent the standard deviation obtained from three independent measurements.

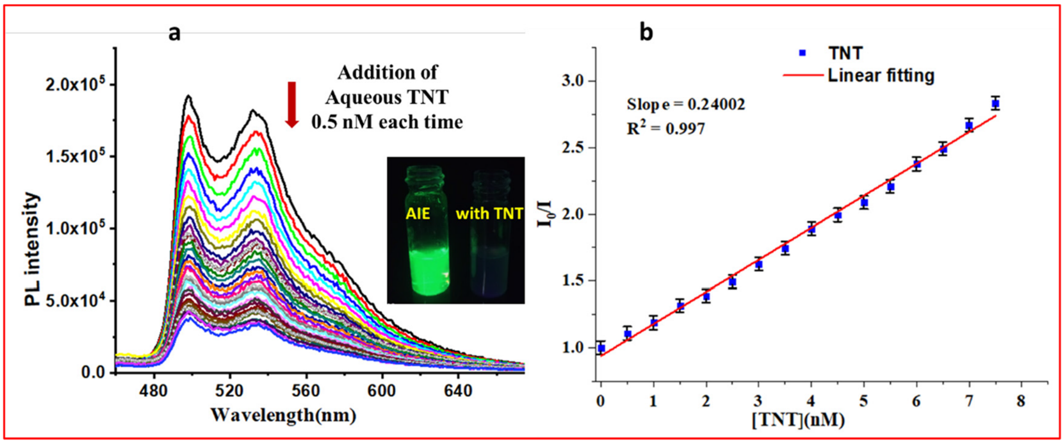

Fig. 5 (a) PL spectra showing the gradual decrease in the photoluminescence (PL) intensity of the AIE solution of **M2** (10^{-3} M THF (10%) and water (90%)) with the continuous addition of aq. TNT (10^{-5} M) 0.5 nM each time. Inset: the 1st vial shows the AIE (90% water) solution of the probe and the 2nd vial shows the aggregate solution of the probe with TNT. (b) Stern–Volmer plot for emission quenching in the case of **M2**; the error bars represent the standard deviation obtained from three independent measurements.

quenching of AIPE-active complexes occurs through dynamic (diffusion) quenching.[25] However, the S–V plot with deviation from linearity was also observed for mixed static/dynamic quenching.[22] Furthermore, to confirm the nature of quenching, we analysed the excited state lifetime study of both complexes in the presence and absence of an analyte (Fig. S23, ESI†). In both cases (**M1** and **M2**), the excited state lifetime values decreased in the presence of TNT analyte, which excluded the possibility of static quenching. No notable difference was observed in the UV-VIS absorbance spectra of the probe and TNT with the absorbance of the sole probe molecule (Fig. S24, ESI†). This observation also neglects the fluorophore (donor) interaction with TNT (acceptor) in the ground state, hence no static quenching could occur.

From these LOD values, we concluded that **M2** is more sensitive towards TNT as compared to **M1**. To investigate the quenching mechanisms, the possibilities of the quenching of emission by the inner filter effect (IFE), resonance energy transfer (RET), and photoinduced electron transfer (PET) have been studied. No overlapping of excitation and emission spectra of **M1** and **M2** was observed, which indicates that there was no IFE present in the prepared complexes (Fig. S25, ESI†). To investigate the possibility of RET, in the case of **M1**, it was observed that there was a slight overlapping of the absorption of TNT and the emission spectrum of **M1** in the same solvent medium (Fig. S26, ESI†), indicating that a possible quenching mechanism for **M1** is RET. The overlapping integral (*J*) calculated using the MATLAB program is 3.94×10^{14}.[66] No such overlap was found in the case of **M2**. The HOMO and LUMO energies of synthesized complexes (Fig. S27, ESI†) were determined to check the possibility of electron transfer from the electron-rich complexes to the electron-deficient TNT. On further analyzing the PET possibilities, we observed that the LUMO level of TNT was −3.49 eV (ref. 67) and for **M1** and **M2**, the LUMO levels were −2.10 eV and −2.82 eV, respectively (Fig. S28, ESI†). From these LUMO alignments, it was observed that electron transfer was more favourable from the LUMO of **M2** to the LUMO of TNT, which led to the quenching of the emission intensity for **M2**.[50,68,69]

The vapor phase detection of nitro-based explosives is a challenging task since the vapor pressure of nitro-explosive is very low (10^{-5}–10^{-15} torr).[24] To detect nitro-explosives in their vapor phase, a very sensitive probe molecule is desirable. The solution phase sensing performances of the complexes (**M1** and **M2**) indicate that **M2** was more sensitive towards TNT (LOD = 450 ppt). To test the probe molecules with TNT vapor, many aspects need to be considered, such as TNT vapor saturation, the selection of a substrate, and the experimental setup for sensing. The experimental setup for TNT vapor sensing is shown in Fig. S29, ESI†. On testing the **M1** and **M2** complexes towards TNT vapors, it was observed that there was no observable decrement in PL intensity with TNT vapor in the case of **M1** (Fig. S30, ESI†). On the other hand, **M2** showed observable PL intensity quenching in the presence of TNT vapor (Fig. 6). The limit of detection (LOD) was found to be 66.3 ppb for **M2**. Although **M1** showed a quenching response in the contact mode detection of TNT, it did not respond to vapors of TNT, which might be due to the lower quantum yield and excited state lifetime of **M1** as compared to **M2** (Table S1, ESI†).

Apart from the mechanism (IFE, RET, and PET) mentioned above, many other factors are responsible for improving the sensitivity in detecting nitro-explosives from vapors, such as the quantum efficiency of the probe molecule, the excited state lifetime of the probe and the porous substrate for trapping vapors of the explosive. Keeping these features in mind, we searched the literature and found some interesting reports from the years 2007 and 2011 regarding the utilization of PMMA polymer as a substrate for improving the photostability and optical properties of metal complexes (quantum yield and excited state lifetime).[70–72] We proceeded with the further improvement of the quantum efficiency of the probe and thus, the probe was embedded in PMMA and tested with TNT vapour to improve the trapping of TNT molecules. First, the composite materials made of complexes (**M1** or **M2**) embedded in PMMA were coated on the filter paper (the detailed method of preparation is described in the Experimental section). After fabricating the probe-PMMA film on filter paper strips, the emission spectra were recorded. Interestingly, the photoluminescence intensity of the embedded film increased drastically as compared to the filter paper containing only the complex (the PL intensity increased up to 4-fold in the case of **M1** and 16-fold in the case of **M2** spectra, as shown in the ESI†, Fig. S31). The QY and lifetimes (Fig. S32, ESI†) of Ir(III) complexes with and without incorporation into the PMMA matrix were recorded and both parameters were enhanced in the complex-embedded polymeric matrix (Table S1, ESI†). The photostability of **M2** and **M2**-PMMA composites (CP) was also studied (Fig. S33 and S34, ESI†). The photostability of **M2** was measured with UV-visible spectra (Fig. S33a) and photoluminescence spectra for 2 hours (Fig. S33b). The experiment indicated that **M2** is photostable. Similarly, the photostability of CP was analysed by UV-VIS and photoluminescence spectra (Fig. S34, ESI†), and it was stable for up to 5 hours under atmospheric conditions. The thermal stability of complexes was investigated by TGA analysis (Fig. S35, ESI†), which showed that both complexes were stable up to ~220 °C. The NMR spectrum of **M2** was recorded after several months and it matched well with the original spectrum of **M2** (Fig. S40, ESI†).

To gain insights into the observed enhanced PL intensity in the presence of PMMA, the surface morphology and porosity of the composite material (CP) were determined. BET data

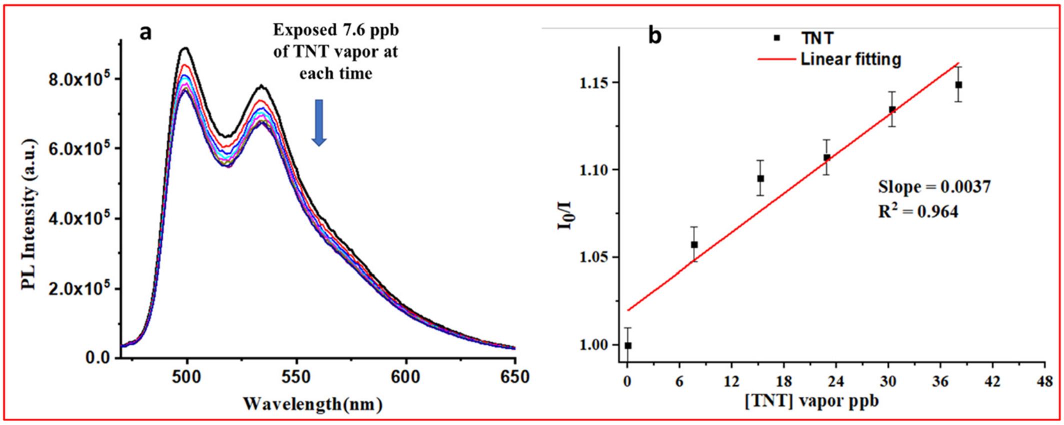

Fig. 6 (a) PL spectra show changes in the photoluminescence (PL) intensities of **M2** on filter paper upon continuous exposure to TNT vapors for 2 min. (b) Stern–Volmer plot for emission quenching in the case of **M2**. The error bars represent the standard deviation obtained from three independent measurements.

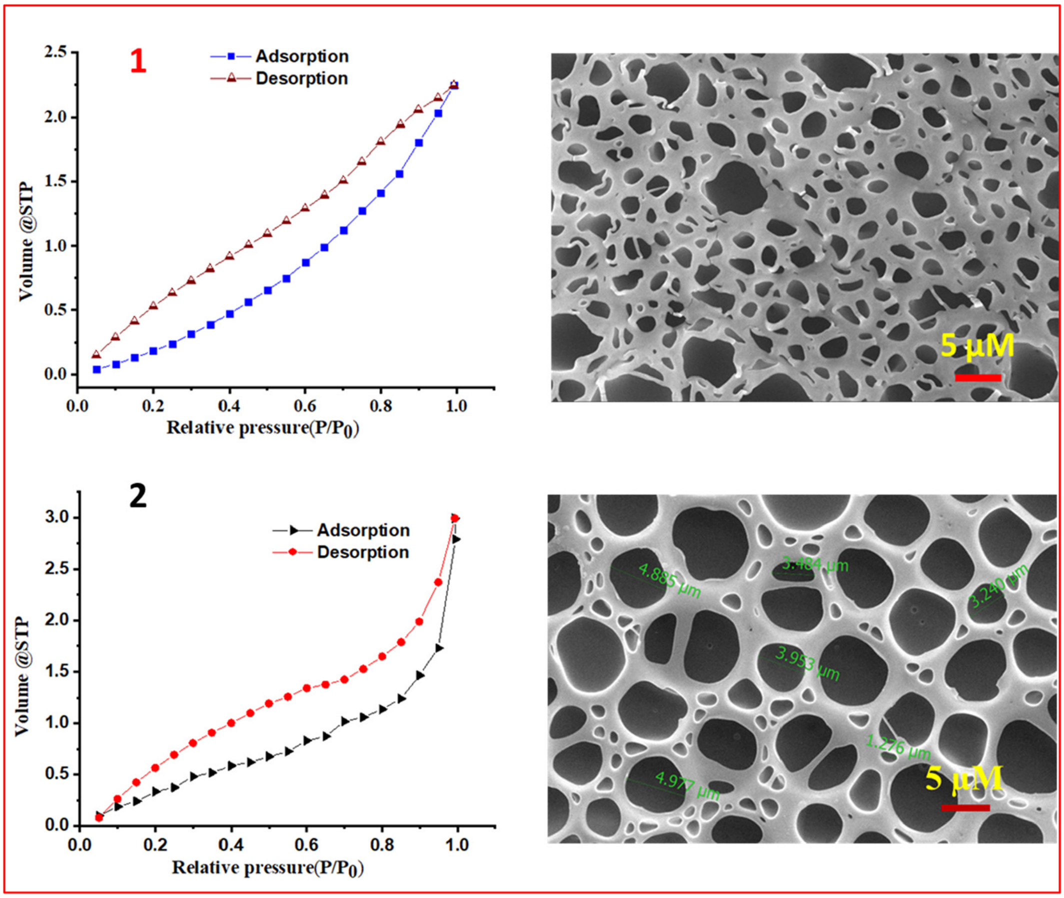

Fig. 7 Nitrogen adsorption–desorption isotherms of the PMMA polymer (**1**) and **M2**-PMMA composite (CP) (**2**) on the left, and corresponding FESEM images on the right.

were obtained and FE-SEM studies of the polymer (PMMA) and CP (Fig. 7) were conducted. The obtained isotherms of CP belong to type IV with an H2(b)-type hysteresis loop at a higher relative pressure.[73–76] The observed H2(b)-type hysteresis loops indicate that the pores are not uniform and are made up of an interconnected network of different sizes. The pore size and the surface area of PMMA and CP were obtained by the Barrett–Joyner–Halenda (BJH) method,[9,77,78] and the surface

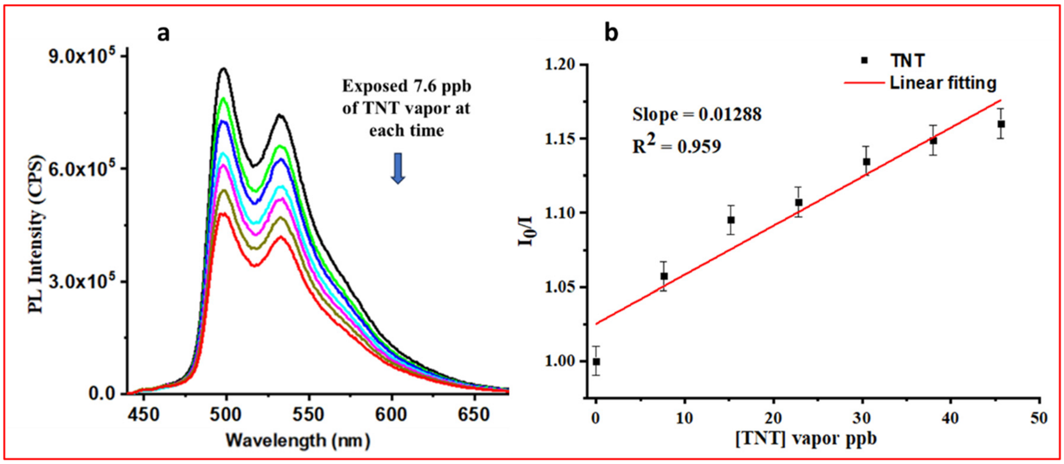

Fig. 8 (a) The decrease in the photoluminescence (PL) intensities of **M2**-PMMA on filter paper upon continuous exposure to TNT vapors for 2 min. (b) Stern–Volmer plot for emission quenching. The error bars represent the standard deviation obtained from three independent measurements.

area for PMMA was found to be 2.944 m^2 g^{-1} with an average pore radius of 2.3407 nm and total pore volume of 0.0034 cc g^{-1}. For CP, the surface area was found to be 2.029 m^2 g^{-1} with an average pore radius of 4.259 nm and a total pore volume of 0.0043 cc g^{-1}. The pore size distributions for PMMA and CP are presented in Fig. S36, ESI†. On analysing the FE-SEM images on thin film for **M2** and CP, it was found that CP showed an interconnected porous network structure (Fig. 7).

After developing the CP with high photostability, quantum efficiency, improved excited state lifetime, and a porous polymeric network, it was tested with TNT vapors and exciting results were obtained as shown in Fig. 8. The CP showed a LOD of 12.8 ppb (limit of detection calculation Fig. S37, ESI†), with ~5 times better quenching efficiency than the **M2** (66.3 ppb). FE-SEM images of PMMA, **M2**, CP, and CP after exposure to TNT are shown in Fig. S38, ESI†. The TNT molecules occupy the pores of the network in CP (Fig. S38, ESI†). The Ir(III) complexes are, in general, highly electron-rich, while trinitrotoluene (TNT) is an electron-deficient molecule. The porous network of CP assisted in trapping the TNT vapor in a polymeric network containing the electron-rich probe (iridium(III) complex, **M2**), which helped to trap TNT effectively, thus enhancing better electronic communication. As a result, significant emission quenching was observed in the case of CP. The essence of the work was to develop a paper strip-based porous polymeric matrix with the AIPE-active iridium(III) complex, which improved the vapor sensing ability of TNT.

4. Conclusion

In summary, an iridium(III)-based monocyclometalated (C^N) phosphorescence sensory material has been developed from a substituted phenyl pyridine ligand. It was strategically planned to impregnate the probes into a porous polymethylmethacrylate (PMMA) polymer. The **M2**-impregnated PMMA resulted in a much higher quantum yield and enhanced lifetime as compared to the sole complex (5-times QY enhancement). PMMA polymer-based films fabricated from the Ir(III) complex have demonstrated compelling efficiency in the detection of explosive vapor. The enhanced quantum efficiency and phosphorescence lifetime of the probe molecule are the essential features of fluorescent sensors and the extended porous morphology allows better interactions of the probe with the analyte. These findings affirm the potential of the present approach, which will be promising for detecting explosives having low vapour pressure in real-time monitoring.

Author contributions

R.P.B: synthesis, conceptualization, methodology, formal analysis, investigation, writing – original draft. A.A: synthesis, formal analysis, calculations, writing – original draft. V.K: conceptualization, methodology, writing – original draft. P.C.R: conceptualization, methodology, writing. IRL: conceptualization, validation, writing – review & editing, supervision, funding acquisition.

Conflicts of interest

There are no conflicts to declare.

Acknowledgements

RPB is gratefully acknowledge Birla Institute of Technology and Science (BITS) Pilani, Pilani campus, Rajasthan (India) for the fellowship. The 'UGC-sponsored Special Assistance Program (F.540/14/DRS/2007, SAP-I)' and DST-FIST Programs in the Chemistry Department are acknowledged for instrumental support. We are obliged to the central instrument facility of BITS Pilani for single crystal, FESEM, BET and other instrumentation facilities. We gratefully acknowledge DRDO, Government of India, for providing nitro-based explosive materials for the sensing study through a research project with project no. ARMREB/CDSW/2019/216.

References

1 K. S. Rao, D. Ganesh, F. Yehya and A. K. Chaudhary, A comparative study of thermal stability of TNT, RDX, CL20 and ANTA explosives using UV 266 nm-time resolved photoacoustic pyrolysis technique, *Spectrochim. Acta, Part A*, 2019, **211**, 212–220.
2 D. M. Dattelbaum, R. S. Chellappa, P. R. Bowden, J. D. Coe and M. A. Margevicius, Chemical stability of molten 2,4,6-trinitrotoluene at high pressure, *Appl. Phys. Lett.*, 2014, **104**(2), 021911.
3 A. Dorsey, C. S. Hodes and P. Richter-Torres, *Toxicological profile for 2, 4, 6-trinitrotoluene*, 1995, pp. 139–171.
4 J. S. Strehse, D. Appel, C. Geist, H.-J. Martin and E. Maser, Biomonitoring of 2, 4, 6-trinitrotoluene and degradation products in the marine environment with transplanted blue mussels (M. edulis), *Toxicology*, 2017, **390**, 117–123.
5 S. Chatterjee, U. Deb, S. Datta, C. Walther and D. K. Gupta, Common explosives (TNT, RDX, HMX) and their fate in the environment: Emphasizing bioremediation, *Chemosphere*, 2017, **184**, 438–451.
6 S. Singh, Sensors—An effective approach for the detection of explosives, *J. Hazard. Mater.*, 2007, **144**(1), 15–28.
7 Y.-Y. Lv, W. Xu, F.-W. Lin, J. Wu and Z.-K. Xu, Electrospun nanofibers of porphyrinated polyimide for the ultra-sensitive detection of trace TNT, *Sens. Actuators, B*, 2013, **184**, 205–211.
8 M. Mäkinen, M. Nousiainen and M. Sillanpää, Ion spectrometric detection technologies for ultra-traces of explosives: A review, *Mass Spectrom. Rev.*, 2011, **30**(5), 940–973.
9 D. Sengottuvelu, V. Kachwal, P. Raichure, T. Raghav and I. R. Laskar, Aggregation-induced enhanced emission (AIEE)-active conjugated mesoporous oligomers (CMOs)

with improved quantum yield and low-cost detection of a trace amount of nitroaromatic explosives, *ACS Appl. Mater. Interfaces*, 2020, **12**(28), 31875–31886.

10 H. A. Yu, J. Lee, S. W. Lewis and D. S. Silvester, Detection of 2,4,6-Trinitrotoluene Using a Miniaturized, Disposable Electrochemical Sensor with an Ionic Liquid Gel-Polymer Electrolyte Film, *Anal. Chem.*, 2017, **89**(8), 4729–4736.

11 S. D. Dongre, T. Das and S. S. Babu, Dual mode selective detection and differentiation of TNT from other nitroaromatic compounds, *J. Mater. Chem. A*, 2020, **8**(21), 10767–10771.

12 W. Dong, Z. Ma, P. Chen and Q. Duan, Carbazole and tetraphenylethylene based AIE-active conjugated polymer for highly sensitive TNT detection, *Mater. Lett.*, 2019, **236**, 480–482.

13 M. Çorman, G. Ozcelikay, A. Cetinkaya, S. Kaya, C. Armutcu, E. Özgür, L. Uzun and S. Ozkan, Metal-organic frameworks as an alternative smart sensing platform for designing molecularly imprinted electrochemical sensors, *TrAC, Trends Anal. Chem.*, 2022, **150**, 116573.

14 M. Boonsri, K. Vongnam, S. Namuangruk, M. Sukwattanasinitt and P. Rashatasakhon, Pyrenyl benzimidazole-isoquinolinones: Aggregation-induced emission enhancement property and application as TNT fluorescent sensor, *Sens. Actuators, B*, 2017, **248**, 665–672.

15 K. K. Kartha, S. S. Babu, S. Srinivasan and A. Ajayaghosh, Attogram sensing of trinitrotoluene with a self-assembled molecular gelator, *J. Am. Chem. Soc.*, 2012, **134**(10), 4834–4841.

16 S.-B. Kim, E.-B. Lee, J.-H. Choi and D.-G. Cho, Simple fluorescent chemosensors for TNT: one-step synthesis, *Tetrahedron*, 2013, **69**(23), 4652–4656.

17 Q. Li, Y.-M. Guo, Y. Gao and G. Li, Polyethyleneimine-protected silver cluster for label-free and highly selective detection of 2, 4, 6-trinitrotoluene, *Spectrochim. Acta, Part A*, 2022, **276**, 121224.

18 S. Moon, J. Yoo, W. Lee and K. Lee, Enhancement of electrochemical detection performance towards 2, 4, 6-trinitrotoluene by a bottom layer of ZnO nanorod arrays, *Heliyon*, 2023, **9**(5), e15880.

19 V. Kumar, B. Maiti, M. K. Chini, P. De and S. Satapathi, Multimodal Fluorescent Polymer Sensor for Highly Sensitive Detection of Nitroaromatics, *Sci. Rep.*, 2019, **9**(1), 7269.

20 M. J. Lefferts and M. R. Castell, Vapour sensing of explosive materials, *Anal. Methods*, 2015, **7**(21), 9005–9017.

21 V. S. Mothika, A. Räupke, K. O. Brinkmann, T. Riedl, G. Brunklaus and U. Scherf, Nanometer-thick conjugated microporous polymer films for selective and sensitive vapor-phase TNT detection, *ACS Appl. Nano Mater.*, 2018, **1**(11), 6483–6492.

22 M. Kumar, V. Vij and V. Bhalla, Vapor-phase detection of trinitrotoluene by AIEE-active hetero-oligophenylene-based carbazole derivatives, *Langmuir*, 2012, **28**(33), 12417–12421.

23 J. I. Steinfeld and J. Wormhoudt, Explosives detection: a challenge for physical chemistry, *Annu. Rev. Phys. Chem.*, 1998, **49**(1), 203–232.

24 X. Sun, Y. Wang and Y. Lei, Fluorescence based explosive detection: from mechanisms to sensory materials, *Chem. Soc. Rev.*, 2015, **44**(22), 8019–8061.

25 B. Prusti and M. Chakravarty, An electron-rich small AIEgen as a solid platform for the selective and ultrasensitive on-site visual detection of TNT in the solid, solution and vapor states, *Analyst*, 2020, **145**(5), 1687–1694.

26 S. Sarkar, Computational design of a nanoconjugate model of pyrene-linked CdTe quantum dot for the detection of trinitrotoluene, *Comput. Theor. Chem.*, 2022, **1211**, 113681.

27 Z.-J. Wang, Q. Li, L.-L. Tan, C.-G. Liu and L. Shang, Metal–organic frameworks-mediated assembly of gold nanoclusters for sensing applications, *J. Anal. Test.*, 2022, **6**(2), 163–177.

28 A. Yildirim, H. Budunoglu, H. Deniz, M. O. Guler and M. Bayindir, Template-free synthesis of organically modified silica mesoporous thin films for TNT sensing, *ACS Appl. Mater. Interfaces*, 2010, **2**(10), 2892–2897.

29 M. S. Zreid, Z. A. Tabasi, X. Ma, T. Wang, M. H. Almatarneh and Y. Zhao, Highly Twisted Aryl–Anthraquinodimethanes: Synthesis, Characterization, and Fluorescence Sensing of TNT, *Eur. J. Org. Chem.*, 2020, **2020**(26), 4031–4041.

30 G. Huang, Q. Li, L. Li and E. Wang, Development of novel polymeric nanoagents and their potential in cancer diagnosis and therapy, *Front. Chem.*, 2022, **10**, 1569.

31 M. Chakraborty, B. Prusti and M. Chakravarty, Small Electron-Rich Isomeric Solid-State Emitters with Variation in Coplanarity and Molecular Packings: Rapid and Ultralow Recognition of TNT, *ACS Appl. Electron. Mater.*, 2022, **4**(5), 2481–2489.

32 T. Naddo, Y. Che, W. Zhang, K. Balakrishnan, X. Yang, M. Yen, J. Zhao, J. S. Moore and L. Zang, Detection of explosives with a fluorescent nanofibril film, *J. Am. Chem. Soc.*, 2007, **129**(22), 6978–6979.

33 B. Xu, X. Wu, H. Li, H. Tong and L. Wang, Selective detection of TNT and picric acid by conjugated polymer film sensors with donor–acceptor architecture, *Macromolecules*, 2011, **44**(13), 5089–5092.

34 P. C. Raichure, R. Bhatt, V. Kachwal, T. C. Sharma and I. R. Laskar, Multi-stimuli distinct responsive D–A based fluorogen oligomeric tool and efficient detection of TNT vapor, *New J. Chem.*, 2022, **46**(14), 6560–6569.

35 V. S. Mothika, A. Räupke, K. O. Brinkmann, T. Riedl, G. Brunklaus and U. Scherf, Nanometer-Thick Conjugated Microporous Polymer Films for Selective and Sensitive Vapor-Phase TNT Detection, *ACS Appl. Nano Mater.*, 2018, **1**(11), 6483–6492.

36 T. K. Ghorpade, A. K. Palai, S. K. Rath, S. K. Sharma, K. Sudarshan, P. K. Pujari, M. Patri and S. P. Mishra, Pentiptycene-tbutylpyrene based poly(arylene-ethynylene)s: Highly sensitive and selective TNT sensor in aqueous as well as vapor phase, *Sens. Actuators, B*, 2017, **252**, 901–911.

37 Q. Zhao, F. Li and C. Huang, Phosphorescent chemosensors based on heavy-metal complexes, *Chem. Soc. Rev.*, 2010, **39**(8), 3007–3030.

38 W. Xu, S. Liu, H. Sun, X. Zhao, Q. Zhao, S. Sun, S. Cheng, T. Ma, L. Zhou and W. Huang, FRET-based probe for fluoride based on a phosphorescent iridium(III) complex containing triarylboron groups, *J. Mater. Chem.*, 2011, **21**(21), 7572–7581.

39 K. M.-C. Wong, W.-S. Tang, X.-X. Lu, N. Zhu and V. W.-W. Yam, Functionalized Platinum(II) Terpyridyl Alkynyl Complexes as Colorimetric and Luminescence pH Sensors, *Inorg. Chem.*, 2005, **44**(5), 1492–1498.

40 H.-Y. Shiu, M.-K. Wong and C.-M. Che, "Turn-on" FRET-based luminescent iridium(III) probes for the detection of cysteine and homocysteine, *Chem. Commun.*, 2011, **47**(15), 4367–4369.

41 A. Agarwal, R. P. Bhatta, V. Kachwal and I. R. Laskar, Controlling the sensitivity and selectivity for the detection of nitro-based explosives by modulating the electronic substituents on the ligand of AIPE-active cyclometalated iridium(III) complexes, *Dalton Trans.*, 2023, **52**, 14182–14193.

42 G. Ge, J. He, H. Guo, F. Wang and D. Zou, Highly efficient phosphorescent iridium(III) diazine complexes for OLEDs: Different photophysical property between iridium(III) pyrazine complex and iridium(III) pyrimidine complex, *J. Organomet. Chem.*, 2009, **694**(19), 3050–3057.

43 C.-H. Yang, Y.-M. Cheng, Y. Chi, C.-J. Hsu, F.-C. Fang, K.-T. Wong, P.-T. Chou, C.-H. Chang, M.-H. Tsai and C.-C. Wu, Blue-Emitting Heteroleptic Iridium(III) Complexes Suitable for High-Efficiency Phosphorescent OLEDs, *Angew. Chem., Int. Ed.*, 2007, **46**(14), 2418–2421.

44 S. J. Lee, K.-M. Park, K. Yang and Y. Kang, Blue Phosphorescent Ir(III) Complex with High Color Purity: fac-Tris(2′,6′-difluoro-2,3′-bipyridinato-N,C4′)iridium(III), *Inorg. Chem.*, 2009, **48**(3), 1030–1037.

45 D.-L. Ma, W.-L. Wong, W.-H. Chung, F.-Y. Chan, P.-K. So, T.-S. Lai, Z.-Y. Zhou, Y.-C. Leung and K.-Y. Wong, A Highly Selective Luminescent Switch-On Probe for Histidine/Histidine-Rich Proteins and Its Application in Protein Staining, *Angew. Chem., Int. Ed.*, 2008, **47**(20), 3735–3739.

46 K. K.-W. Lo, K. Y. Zhang, S.-K. Leung and M.-C. Tang, Exploitation of the Dual-emissive Properties of Cyclometalated Iridium(III)–Polypyridine Complexes in the Development of Luminescent Biological Probes, *Angew. Chem., Int. Ed.*, 2008, **47**(12), 2213–2216.

47 Sumit, K. S. Maravajjala, S. Khanna, V. Kachwal, K. L. Swetha, S. Manabala, R. Chowdhury, A. Roy and I. R. Laskar, Rational Molecular Designing of Aggregation-Enhanced Emission (AEE) Active Red-Emitting Iridium(III) Complexes: Effect of Lipophilicity and Nanoparticle Encapsulation on Photodynamic Therapy Efficacy, *ACS Appl. Bio Mater.*, 2023, **6**(4), 1445–1459.

48 S. W. Park, H. W. Ham and Y. S. Kim, Theoretical Studies of Mono-Cyclometalated Ir(III) Complexes with Phenylpyrazole Based Ligands and Phosphines, *Mol. Cryst. Liq. Cryst.*, 2011, **551**(1), 24–32.

49 M. S. Lowry and S. Bernhard, Synthetically Tailored Excited States: Phosphorescent, Cyclometalated Iridium(III) Complexes and Their Applications, *Chem. – Eur. J.*, 2006, **12**(31), 7970–7977.

50 K. S. Bejoymohandas, T. M. George, S. Bhattacharya, S. Natarajan and M. L. P. Reddy, AIPE-active green phosphorescent iridium(III) complex impregnated test strips for the vapor-phase detection of 2,4,6-trinitrotoluene (TNT), *J. Mater. Chem. C*, 2014, **2**(3), 515–523.

51 P. Alam, G. Kaur, V. Kachwal, A. Gupta, A. R. Choudhury and I. R. Laskar, Highly sensitive explosive sensing by "aggregation induced phosphorescence" active cyclometalated iridium(III) complexes, *J. Mater. Chem. C*, 2015, **3**(21), 5450–5456.

52 P. Alam, M. Karanam, A. R. Choudhury and I. R. Laskar, One-pot synthesis of strong solid state emitting mono-cyclometalated iridium(III) complexes: study of their aggregation induced enhanced phosphorescence, *Dalton Trans.*, 2012, **41**(31), 9276–9279.

53 E. Longhi and L. De Cola, Iridium(III) complexes for OLED application, in *Iridium(III) in optoelectronic and photonics applications*, 2017, pp. 205–274.

54 T.-Y. Li, J. Wu, Z.-G. Wu, Y.-X. Zheng, J.-L. Zuo and Y. Pan, Rational design of phosphorescent iridium(III) complexes for emission color tunability and their applications in OLEDs, *Coord. Chem. Rev.*, 2018, **374**, 55–92.

55 K. K.-W. Lo and K. Y. Zhang, Iridium(III) complexes as therapeutic and bioimaging reagents for cellular applications, *RSC Adv.*, 2012, **2**(32), 12069–12083.

56 W. J. Hehre, R. Ditchfield and J. A. Pople, Self—consistent molecular orbital methods. XII. Further extensions of Gaussian—type basis sets for use in molecular orbital studies of organic molecules, *J. Chem. Phys.*, 1972, **56**(5), 2257–2261.

57 M. Frisch, G. Trucks, H. B. Schlegel, G. Scuseria, M. Robb, J. Cheeseman, G. Scalmani, V. Barone, G. Petersson and H. Nakatsuji, *Gaussian 16*, Gaussian, Inc., Wallingford, CT, 2016.

58 L. E. Roy, P. J. Hay and R. L. Martin, Revised basis sets for the LANL effective core potentials, *J. Chem. Theory Comput.*, 2008, **4**(7), 1029–1031.

59 Rigaku, *CrysAlisPro Software System, Version 1.171.38.41, Rigaku Oxford Diffraction*, 2015, https://www.rigaku.com.

60 O. V. Dolomanov, L. J. Bourhis, R. J. Gildea, J. A. Howard and H. Puschmann, OLEX2: a complete structure solution, refinement and analysis program, *J. Appl. Crystallogr.*, 2009, **42**(2), 339–341.

61 G. M. Sheldrick, Crystal structure refinement with SHELXL, *Acta Crystallogr., Sect. C: Struct. Chem.*, 2015, **71**(1), 3–8.

62 P.-N. Lai, C. H. Brysacz, M. K. Alam, N. A. Ayoub, T. G. Gray, J. Bao and T. S. Teets, Highly Efficient Red-Emitting Bis-Cyclometalated Iridium Complexes, *J. Am. Chem. Soc.*, 2018, **140**(32), 10198–10207.

63 S. Sprouse, K. A. King, P. J. Spellane and R. J. Watts, Photophysical effects of metal-carbon .sigma. bonds in ortho-metalated complexes of iridium(III) and rhodium(III), *J. Am. Chem. Soc.*, 1984, **106**(22), 6647–6653.

64 J. C. Deaton, C. M. Taliaferro, C. L. Pitman, R. Czerwieniec, E. Jakubikova, A. J. Miller and F. N. Castellano, Excited-state switching between ligand-centered and charge transfer modulated by metal–carbon bonds in cyclopentadienyl

iridium complexes, *Inorg. Chem.*, 2018, **57**(24), 15445–15461.

65 L. Ravotto and P. Ceroni, Aggregation induced phosphorescence of metal complexes: From principles to applications, *Coord. Chem. Rev.*, 2017, **346**, 62–76.

66 S. Muthusubramanian and S. K. Saha, Exploration of twisted intramolecular charge transfer fluorescence properties of trans-2-[4-(dimethylamino) styryl] benzothiazole to characterize the protein–surfactant aggregates, *J. Lumin.*, 2012, **132**(8), 2166–2177.

67 J. V. Prata, A. I. Costa and C. M. Teixeira, A Solid-State Fluorescence Sensor for Nitroaromatics and Nitroanilines Based on a Conjugated Calix[4]arene Polymer, *J. Fluoresc.*, 2020, **30**(1), 41–50.

68 N. Jiang, G. Li, W. Che, D. Zhu, Z. Su and M. R. Bryce, Polyurethane derivatives for highly sensitive and selective fluorescence detection of 2,4,6-trinitrophenol (TNP), *J. Mater. Chem. C*, 2018, **6**(42), 11287–11291.

69 G. Wang, M. Li, Q. Wei, Y. Xiong, J. Li, Z. Li, J. Tang, F. Wei and H. Tu, Design of an AIE-Active Flexible Self-Assembled Monolayer Probe for Trace Nitroaromatic Compound Explosive Detection, *ACS Sens.*, 2021, **6**(5), 1849–1856.

70 C. N. Fleming, D. M. Dattelbaum, D. W. Thompson, A. Y. Ershov and T. J. Meyer, Excited State Intervalence Transfer in a Rigid Polymeric Film, *J. Am. Chem. Soc.*, 2007, **129**(31), 9622–9630.

71 D. W. Thompson, C. N. Fleming, B. D. Myron and T. J. Meyer, Rigid Medium Stabilization of Metal-to-Ligand Charge Transfer Excited States, *J. Phys. Chem. B*, 2007, **111**(24), 6930–6941.

72 X. Wang, S. Xu and W. Xu, Luminescent properties of dye-PMMA composite nanospheres, *Phys. Chem. Chem. Phys.*, 2011, **13**(4), 1560–1567.

73 M. Myilsamy, M. Mahalakshmi, N. Subha and V. Murugesan, Mesoporous Ga–TiO2: Role of Oxygen Vacancies for the Photocatalytic Degradation Under Visible Light, *J. Nanosci. Nanotechnol.*, 2018, **18**(2), 925–935.

74 G. Rasines, C. Macías, M. Haro, J. Jagiello and C. O. Ania, Effects of CO2 activation of carbon aerogels leading to ultrahigh micro-meso porosity, *Microporous Mesoporous Mater.*, 2015, **209**, 18–22.

75 X. Zhou, X. Cheng, W. Feng, K. Qiu, L. Chen, W. Nie, Z. Yin, X. Mo, H. Wang and C. He, Synthesis of hollow mesoporous silica nanoparticles with tunable shell thickness and pore size using amphiphilic block copolymers as core templates, *Dalton Trans.*, 2014, **43**(31), 11834–11842.

76 M. Thommes, K. Kaneko, A. V. Neimark, J. P. Olivier, F. Rodriguez-Reinoso, J. Rouquerol and K. S. Sing, Physisorption of gases, with special reference to the evaluation of surface area and pore size distribution (IUPAC Technical Report), *Pure Appl. Chem.*, 2015, **87**(9–10), 1051–1069.

77 Z. U. Rahman, N. Wei, Z. Li, W. Sun and D. Wang, Preparation of hollow mesoporous silica nanospheres: Controllable template synthesis and their application in drug delivery, *New J. Chem.*, 2017, **41**(23), 14122–14129.

78 J. Jeromenok and J. Weber, Restricted access: on the nature of adsorption/desorption hysteresis in amorphous, microporous polymeric materials, *Langmuir*, 2013, **29**(42), 12982–12989.